ACS APPLIED MATERIALS & INTERFACES

www.acsami.org

Research Article

Overcoming Ion Trapping in Chevrel Phase Compounds via Tailored Anion Substitution: An Integrated Study of Theory, Synthesis, and In Operando Techniques for Reversible Aqueous Zn-Ion Batteries

Yuanshen Wang, Katharina Helmbrecht, Weihao Li, Manuel Dillenz, Yejun Wang, Axel Groß,* and Alexey Y. Ganin*

Cite This: ACS Appl. Mater. Interfaces 2024, 16, 50671−50678

Read Online

ACCESS | Metrics & More | Article Recommendations | Supporting Information

ABSTRACT: Sustainable batteries are key for powering electronic devices of the future, with aqueous zinc-ion batteries (AZIBs) standing out for their use of abundant, readily available elements, and safer production processes. Among the various electrode materials studied for AZIBs, the Chevrel Phase, Mo_6S_8 has shown promise due to its open framework, but issues with zinc ion trapping have limited its practical application. In this work, we employed computational methods to investigate the insertion-deinsertion mechanism in a series of isostructural $Mo_6S_{8-x}Se_x$ (x = 0−8) solid solutions as materials that could balance the gravimetric capacity and reversible cycling for AZIBs. Density functional theory (DFT) calculations revealed that increasing the Se content would reduce the binding energy of Zn within the structures, enabling Zn deinsertion compared to the Mo_6S_8 structure. Experiments confirmed the formation of $Mo_6S_{8-x}Se_x$ (x = 0−8) solid solutions, and electrochemical testing showed improved reversibility of Zn insertion/deinsertion as the amount of Se increased, consistent with the computational predictions. Furthermore, combined in operando X-ray diffraction and electrochemical studies revealed a continuous, gradual Zn-insertion process into $Mo_6S_4Se_4$, in stark contrast to the abrupt phase changes observed upon Zn insertion in Mo_6S_8 and Mo_6Se_8. DFT calculations attributed the stabilization of $Zn_{0.5}Mo_6S_4Se_4$ as a prime reason for preventing phase separation, making Se-substituted compounds promising materials for high-performance AZIBs. Overall, this interdisciplinary approach, integrating computational modeling, materials synthesis, and advanced characterization techniques, offers a pathway for fine-tuning anion chemistry that can help create high-performance electrode materials for sustainable energy storage technologies.

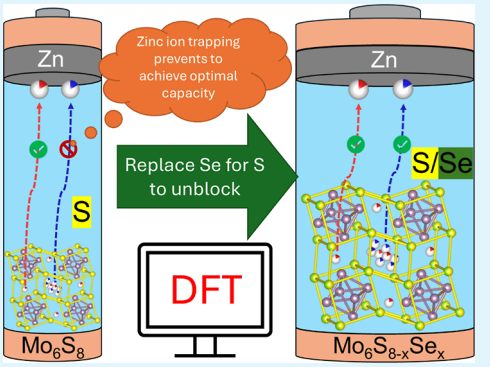

KEYWORDS: *zinc-ion battery, computational materials design, solid-state solutions, in operando battery characterization, powder X-ray diffraction*

INTRODUCTION

Sustainable batteries are key for powering the electronic devices of the future. Aqueous zinc-ion batteries (AZIBs) are particularly promising for this role as they are made from abundant and readily available elements.[1] Furthermore, as none of the components are significantly moisture or air sensitive, their production can be safer and cheaper than, for example, that of lithium-ion batteries (LIBs).[2,3] Moreover, in AZIBs zinc metal is utilized directly as the anode material, enabling a high specific volumetric capacity that makes them well-suited for portable and mobile devices where a high energy density in a limited space is required. However, despite significant progress over the past decade, the research in AZIBs is still in its infancy compared with the advances in more established LIB systems.

There is a range of electrode materials studied for the application of AZIBs. Among those many studied to date, a particularly curious case stands out. Mo_6S_8 (which is often referred as the Chevrel phase) has a crystal structure that features a highly open framework.[4] The framework enables short ion transporting pathways and makes Mo_6S_8 a promising material for AZIBs.[5] Consequently, recent work demonstrated that in aqueous electrolyte, the Mo_6S_8 cathode reached a very reasonable capacity of 134 mA h g^{-1} on the first discharge.[6] The cathode showed two discharge plateaus at around 0.5 and 0.35 V due to electrochemical insertion of Zn^{2+} into Mo_6S_8 upon formation of $ZnMo_6S_8$ and $Zn_2Mo_6S_8$. However, there was a significant capacity loss upon further cycling. This was due to zinc-ion trapping, which prevented deinsertion from

Received: June 3, 2024
Revised: September 2, 2024
Accepted: September 2, 2024
Published: September 13, 2024

proceeding beyond $ZnMo_6S_8$ to fully deinserted Mo_6S_8. Similar electrochemical behavior, resulting in a significant capacity loss (and confirming that it was impossible to deinsert $ZnMo_6S_8$ fully back to the original Mo_6S_8) was reported by other researchers.[7] This loss of capacity makes Mo_6S_8 an unattractive material for AZIBs.

On the other hand, in their recent work Levi et al. have shown that Mg^{2+} ion trapping does not occur within the parental Mo_6Se_8 compound (which is isostructural with Mo_6S_8).[8] The trapping was avoided because of the higher polarizability of Se^{2-} anions within the crystal structure of Mo_6Se_8. A recent theoretical study elucidated the role of different charge carriers in AZIBs and revealed that a direct relation between the ionic radii and the diffusion barriers of Zn and Mg within the Chevrel phase causes both ions to act similarly in Mo_6Se_8.[9] Indeed, the very recent work showcased the reversibility of Zn^{2+} insertion/deinsertion into Mo_6Se_8, leading to a fully reversible AZIB.[10] Remarkably, the authors suggested that the highly reversible nature of the insertion process into Mo_6Se_8 was due to the fact that within the crystal structure, the isolated $\{Mo_6\}$ metal clusters remained redox-inert upon the electrochemical process of Zn-ion insertion. Thus, the electrochemical process proceeds without significant altering of the metal bonding and hence preserves the crystal structure integrity, suggesting an opportunity for a highly stable battery. While Mo_6Se_8 shows reversibility for Zn insertion/deinsertion, it may not be an optimal electrode material for AZIBs due to its lower theoretical gravimetric capacity compared to Mo_6S_8. Tuning the sulfur-to-selenium ratio through rational design of the material's composition and structure could allow balancing the gravimetric capacity and reversible cycling.

In this work, we employed computational methods to understand the mechanism of insertion in a series of solid-state solutions between Mo_6S_8 and Mo_6Se_8. Building on our previous studies performed on the Chevrel phases, the research revealed that increasing the Se content within $Mo_6S_{8-x}Se_x$ (x = 0−8) solid solutions would reduce the binding energy of Zn within their structures, enabling Zn deinsertion compared to Mo_6S_8.[9] Complementary experimental work and characterization confirmed the formation of $Mo_6S_{8-x}Se_x$ solid solutions. Electrochemical testing showed that reversibility of Zn insertion/deinsertion improves within the solid solutions as the amount of Se increases consistent with density functional theory (DFT) computations. In operando X-ray diffraction studies showed that $Mo_6S_4Se_4$ exhibits a gradual shift of the key peak positions (rather than abrupt phase changes observed in Mo_6S_8 and Mo_6Se_8), suggesting that $Mo_6S_4Se_4$ behaves differently electrochemically from the end members in this solid solution series. These findings demonstrate the importance of tailoring the anion chemistry within Chevrel compounds for achieving efficient multivalent ion insertion in AZIBs.

EXPERIMENTAL METHODS

Synthesis of $Mo_6S_{8-x}Se_x$ (x = 0, 2, 4, 6, and 8). The targeted compounds were prepared by deinsertion of Cu from the corresponding $Cu_2Mo_6S_{8-x}Se_x$ (x = 0, 2, 4, 6, and 8) powders which were prepared as described in detail in Supporting Information Note 1.[6] In a typical reaction, 300 mg of $Cu_2Mo_6S_{8-x}Se_x$ (x = 0, 2, 4, 6, and 8) powder was added to 30 mL of 0.5 M $Fe(NO_3)_3$ solution and stirred at 400 rpm for 24 h. The resulting powder was isolated by filtration under vacuum, washed with copious amounts of distilled water, and finally dried at 60 °C overnight. All handling was carried out under ambient conditions without recourse to a protective atmosphere.

Electrochemical Measurements. $Cu_2Mo_6S_{8-x}Se_x$, Super P carbon black (CB, Alfa Aesar, ≥99%), and polyvinylidene difluoride (PVDF, Aldrich) were mixed in a weight ratio of 7:2:1 (total mass 50 mg) and ground with a pestle and mortar, followed by the addition of 240 μL of *N*-methyl-2-pyrrolidone (NMP, Sigma-Aldrich, ≥99%). The mixture was ground thoroughly until a uniform black slurry was formed. The slurry was coated onto aluminum foil using a 20 μm coater and dried at 60 °C overnight. Disks with an area of ca. 1.057 cm^2 (diameter of 1.16 cm) were punched from the foil corresponding to the average loading of the mixture on the foil at 1.14 $mg{\cdot}cm^{-2}$ (corresponding to 0.798 $mg{\cdot}cm^{-2}$ of the active Chevrel phase material). A zinc foil (Merck, 99.9%) disk with an area of ca. 1.057 cm^2 (diameter 1.16 cm, thickness 0.25 cm) served as an anode.

Battery tests were carried out in two types of battery cells at ambient temperature of ca. 18 °C. Swagelok cells were routinely used for all experiments except for in operando XRD studies, as discussed below. The cells were assembled by sandwiching a glass fiber membrane (Whatman GF/A, diameter 13.94 mm, thickness 0.26 mm) wetted with 60 μL of 1 M $ZnSO_4$ aqueous solution between two electrodes. Cells were assembled following the order of anode shell, spring, current collector, zinc disk anode, separator, soaking electrolyte, cathode disk, and then cathode shell. For the in operando XRD studies, the CR2032 type cell with the identical cathode, separator, and Zn-metal anode was used but with a window made from Kapton on the cathode side to allow the beam transmittance. Cyclic voltammetry (CV) and galvanostatic charge−discharge (GCD) techniques were conducted on a Biologic, SP-150 (EC-laboratories) potentiostat and a Lanhe battery cycler, respectively.

Powder X-ray Diffraction Studies. Powder samples were measured on a Rigaku MiniFlex 6G diffractometer (Cu $K_{\alpha1}$ and Cu $K_{\alpha2}$ wavelengths, 1.5406 and 1.5444 Å, respectively) equipped with a D/teX Ultra detector and operating in the Bragg−Brentano geometry. Powder samples were carefully packed onto zero background holders and leveled using a glass microscope slide. The sample holder was spun at a rate of 10 rpm during the measurement. The patterns were collected at a step size of 0.015° and scan rate of 3°/min. In operando X-ray diffraction studies coupled with battery testing were carried out on a Malvern PANalytical Empyrean operating in the Bragg−Brentano geometry using an XRD holder (Malvern PANanlytical, Cu $K_{\alpha1}$ and Cu $K_{\alpha2}$ wavelengths, 1.5406 and 1.5444 Å, respectively) that was designed for a CR2032 coin cell. The diffraction patterns were collected with a step size of 0.013° and scan rate of 4°/min at a repeated scan mode without spin. The crystal structures were refined using GSAS-II software by the Rietveld method.

Microscopy Studies. For scanning electron microscopy/energy-dispersive X-ray (SEM/EDX) studies, a small amount of sample powder was attached to sticky carbon tape, which was shaken to remove excess powder. The tape was attached to an Al holder. Morphology studies were carried out on a scanning electron microscope (TESCAN CLARA) equipped with a Field Emission Gun electron source, which was coupled with an Oxford Instruments UltimMax 65 with an Aztec live interface EDX system for elemental analysis. The particle size distribution has been evaluated using Nanomeasurer software (Informer Technologies), with ∼200 particles used for the evaluation of each sample.

Theoretical Calculations. The properties of the materials as well as the ion migration of Zn inside the phase were studied using periodic DFT,[11,12] as implemented in the Vienna ab initio simulation package.[13−15] The generalized gradient approximation in the formulation of Perdew, Burke, and Ernzerhof (PBE) was used,[16] as has been carried out in many DFT studies addressing properties of the Chevrel phase before,[9,17] as well as the revised PBE functional in combination with the Grimme D3 correction applied.[18,19] It has also been shown that using the revised PBE functional with a Grimme correction for dispersion forces gives superior results in some cases,[9] and this approach was thus used for some calculations, which are specified in the main text. Calculations were first performed for the solid solution unit cell of the Chevrel phase with the Brillouin zone

https://doi.org/10.1021/acsami.4c09145
ACS Appl. Mater. Interfaces 2024, 16, 50671−50678

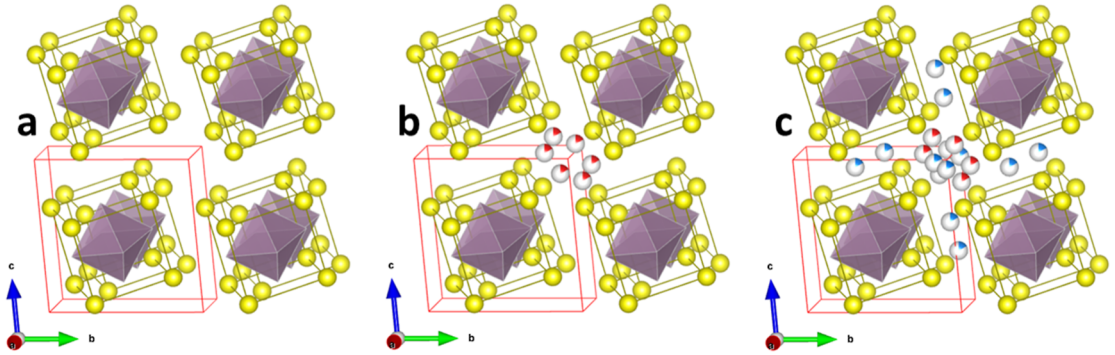

Figure 1. Crystal structures of (a) Mo_6S_8, (b) $ZnMo_6S_8$, and (c) $Zn_2Mo_6S_8$ consisting of Mo_6S_8 blocks with Zn-ions taking the cavity positions between them. Mo—magenta, S—yellow, Zn1—gray/red, and Zn2—gray/blue. The unit cell is displayed in red solid line.

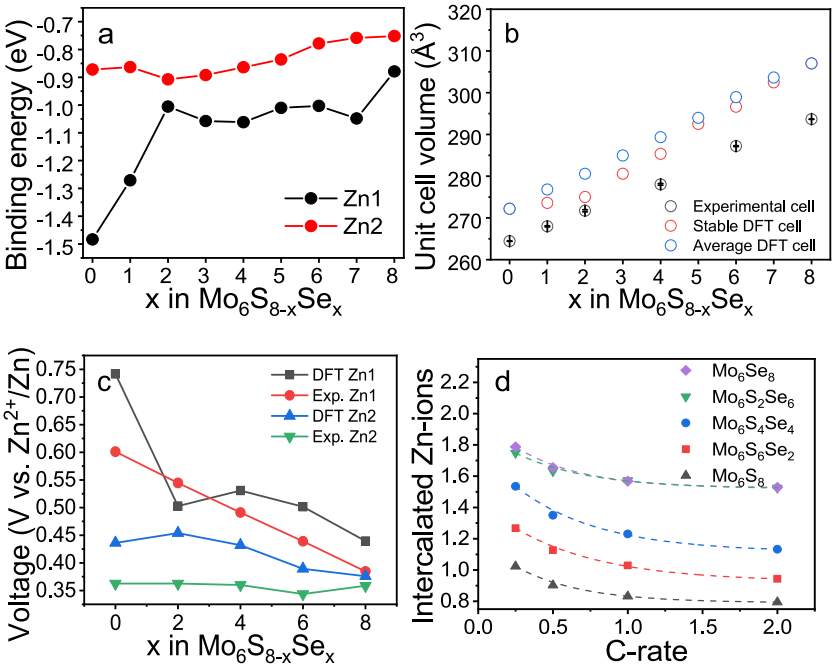

Figure 2. (a) Binding energy of Zn1 and Zn2 in the most stable configuration across $Mo_6S_{8-x}Se_x$ solid solutions as a function of the Se content. (b) Comparison of the unit cell volumes (normalized to the reduced primitive cell) of $Mo_6S_{8-x}Se_x$ from the Rietveld refinement and DFT calculations. (c) Insertion voltage of Zn1 and Zn2 into $Mo_6S_{8-x}Se_x$ structures calculated by DFT and determined experimentally. (d) Rate performance of $Mo_6S_{8-x}Se_x$ at 0.25, 0.5, 1, and 2 C, the number of inserted Zn was calculated from the third cycle's data.

sampled using an 8 × 8 × 8 *k*-point grid. For insertion and ion diffusion, different supercells (which are specified in the respective sections) were used, and the *k*-point grid was scaled accordingly in each lattice direction. The electronic structure was converged to 1×10^{-4} eV, with a plane-wave cutoff energy of 450 eV.

RESULTS AND DISCUSSION

Computational Work. As first-principles calculations have been shown to be a viable tool to derive battery properties before,[20] we took a computational approach to identify the theoretical battery performance. Mo_6S_8 and Mo_6Se_8 are isostructural compounds and form a series of homogeneous solid solutions.[21] Therefore, to build $Mo_6S_{8-x}Se_x$ models, we used the Mo_6S_8 structure as a basis, incrementally exchanging S with Se. The potential sites for the insertion of Zn ions within the Mo_6S_8 structure are shown in Figure 1. There are two different sites within the structure that are available for the insertion of Zn ions yielding the chemical formulas $ZnMo_6S_8$ and $Zn_2Mo_6S_8$, respectively.

Notably, there are two insertion sites for zinc in Mo_6S_8, and each site forms a ring. The first one is the more stable inner ring, while the second site is the less stable outer ring. Within each of these rings, the zinc sites are partly occupied. Each site is only partly occupied to 1/6, creating a significant challenge in describing of structural model using DFT. There are numerous configurations with regard to each of these six partially occupied sites. In addition, there are 720 additional configurations within the combined two-zinc position unit cell, making calculations extremely challenging in terms of computation.

To address this challenge, we followed a previously described approach[9] and adopted a reduced unit cell (Figures S1−S3) that is still representative of the original crystal structure (Figure 1) since the chemical environment of all atoms is preserved. Due to the equivalency of Zn ions within "the rings" (as discussed at length in our previous paper),[9] specific positions of the zinc ions can be chosen within the inner and outer rings, respectively. Therefore, it is possible to

https://doi.org/10.1021/acsami.4c09145
ACS Appl. Mater. Interfaces 2024, 16, 50671−50678

define the position of Mo and S solely with respect to the Zn1 site and the [Mo_6S_8] cluster (Figure S2). Similarly, in $Zn_2Mo_6S_8$, the [Mo_6S_8] cluster and Zn1 site remain, while an additional Zn2 is added (Figure S3).

The reduced cell allowed us to build a range of possible crystal structures, describing numerous configurations within $Mo_6S_{8-x}Se_x$ solid solutions. Consequently, depending on the Se content, the number of the possible configurations can be resolved through a combinatorial approach (Table S1). The number of possible configurations for a given composition within $Mo_6S_{8-x}Se_x$ (x = 1−8) depends on the S/Se ratio. For example, in the case of $Mo_6S_7Se_1$, there are eight different configurations, in the case of $Mo_6S_6Se_2$, there are 28 possible variations, and so on.

The optimization for the most stable $Mo_6S_{8-x}Se_x$ configurations of the reduced unit cell were carried out using the revised PBE functional in combination with the Grimme D3 correction (RPBE + D3) functional (see Supporting Information Note 1 for more details). The most stable configurations (for a given Se content) are displayed in Figures S4−S10, while their calculated unit cell parameters are summarized in Table S2. The parameters follow a linear trend, which is expected for the formation of solid solutions.

The binding energies of Zn1 and Zn2 ions within the most stable configurations are plotted in Figure 2a as a function of Se content.

In addition, Figure S11 shows binding energies for all possible configurations of the crystal structures. It should be noted that the binding energies in Figure 2a are derived with RPBE + D3, while all PBE values show the same trend (Figure S11). In previous research,[9] PBE provides the closest lattice parameters than RPBE + D3, but underestimate the energy (as well as insertion voltages), where RPBE + D3 was opposite. However, the difference in the specific value will not affect the energy/lattice parameters/insertion voltage trends in $Mo_6S_{8-x}Se_x$ solid solution systems. Since Mo_6S_8 and Mo_6Se_8 were selected as references, the consistency of the trend of the solid solution energy change in the PBE function and the RPBE + D3 function proves that there are no unconsidered parameters in the system.

Previous experimental data showed that during the initial electrochemical process two Zn ions would insert into Mo_6S_8 upon formation of $Zn_2Mo_6S_8$.[6,7] However, upon discharge, only one Zn can be deinserted from the $Zn_2Mo_6S_8$. Hence, the deinsertion does not proceed beyond $ZnMo_6S_8$, preventing the reversibility of Mo_6S_8 and dramatically reducing the battery capacity. The inability of Zn to deinsert from $ZnMo_6S_8$ is due to a large binding energy of Zn1 ions within the Mo_6S_8 structure (Figure 2a). However, as S is gradually replaced with Se in $Mo_6S_{8-x}Se_x$, the binding energy of Zn1 is reduced drastically. In particular, the binding energy of Zn1 drops sharply from −1.48 eV in Mo_6S_8 to −1.01 eV in $Mo_6S_6Se_2$ and stays consistent around −1.00 eV for the remaining solid solutions until finally reaching −0.88 eV for Mo_6Se_8. This suggests that replacing S with Se would lead to a more facile deinsertion of Zn1. Finally, a closer examination of the binding energies (Figure S11) reveals that the location of the Se sites within the reduced unit cell plays a role, but it is evident that the Zn binding energy follows a downward trend consistent with the replacement of S by Se.

Synthesis and Characterization of $Mo_6S_{8-x}Se_x$ (x = 0, 2, 4, 6, and 8). Since DFT calculations predicted that replacing S with Se in Mo_6S_8 would lead to an improved deinsertion process, five $Mo_6S_{8-x}Se_x$ solid solutions with x = 0, 2, 4, 6, and 8 were synthesized (see Supporting Information Note 1 and Experimental Methods). The Rietveld refinement of the crystal structure model based on Mo_6S_8 (space group: $R\bar{3}m$)[22] against the experimental PXRD data (Figures S12−S16) showed a good match between the experimental and calculated profiles. In the case of Mo_6Se_8, the final profile (Figure S16) revealed some unfitted peaks which were consistent with the presence of a small impurity of hexagonal $MoSe_2$.[23] The refined unit cell volumes of the experimentally prepared phases showed a near linear trend confirming the formation of a series of solid solutions in line with Vegard's law (Figure 2b). The structural parameters obtained from the Rietveld refinement for $Mo_6S_{8-x}Se_x$ are summarized in Table S3. There is good agreement with the previously reported crystal data in the literature especially for the two end members of the series: Mo_6S_8 and Mo_6Se_8.[6,24,25] However, due to the expected random distribution of S and Se within the relevant $Mo_6S_{x-8}Se_x$ crystal structure, the experimental unit cell volumes deviate from the most stable energy configurations obtained by DFT (which assumed the fixed position of the S or Se within the cell). However, when the average unit cell volumes are considered over all configurations, the linear trend of the calculated volumes is restored and remains consistent with the experimental unit cell volumes (Figure 2b). The powder diffraction patterns of the synthesized samples (Figure S17) showed a gradual shift of the reflections toward lower angles which is consistent with the increased unit cell volume and the replacement of S with Se within the crystal structure.

As the difference in particle sizes between the samples can cause variability in the electrochemical performance,[26] the particle size distributions across $Mo_6S_{8-x}Se_x$ (x = 0, 2, 4, 6, and 8) were evaluated by SEM microscopy (Figure S18). There is significant variation in particle sizes within each sample, ranging from 0.5 to 4.8 μm. However, across all prepared samples, the morphology remains relatively consistent, as evidenced by average particle sizes ranging between 1.43 and 1.63 μm (Figure S19). This ensures that the electrochemical performance across the samples is not influenced by the particle sizes. Finally, the EDX (with representative spectra displayed in Figure S20) confirmed that the samples were fully deinserted and confirmed the absence of peaks associated with Cu or Fe. The compositions of the experimental samples were close to the expected ones as well confirming a good agreement with the expected ratios (Table S4).

Zn-Ion Battery Performance of $Mo_6S_{8-x}Se_x$ (x = 0, 2, 4, 6, and 8). A series of CV experiments were carried out (Figures 3 and S21, S22) to probe the effect of the S substitution for Se within $Mo_6S_{8-x}Se_x$. During the first negative scan, Mo_6S_8 displays two distinctive cathodic peaks at ∼0.32 and ∼0.40 V vs Zn^{2+}/Zn corresponding to the insertion of two Zn ions upon formation of $ZnMo_6S_8$ and $Zn_2Mo_6S_8$, respectively. However, upon the reverse scan, only the peak at ∼0.40 V remains, suggesting that the deinsertion of Zn from $ZnMo_6S_8$ is impeded. These observations for Mo_6S_8 are consistent with the previous research.[6]

Notably, the substitution of S with Se enables the Zn deinsertion process, as evident from the presence of two peaks in the cycling voltammetry data. For example, the close analysis of the CV data suggests that the insertion into $Mo_6S_4Se_4$ (Figure 3c) and $Mo_6S_2Se_6$ is fully reversible (Figure S22). However, there is a distinctive broadening of the peaks of the

https://doi.org/10.1021/acsami.4c09145
ACS Appl. Mater. Interfaces 2024, 16, 50671−50678

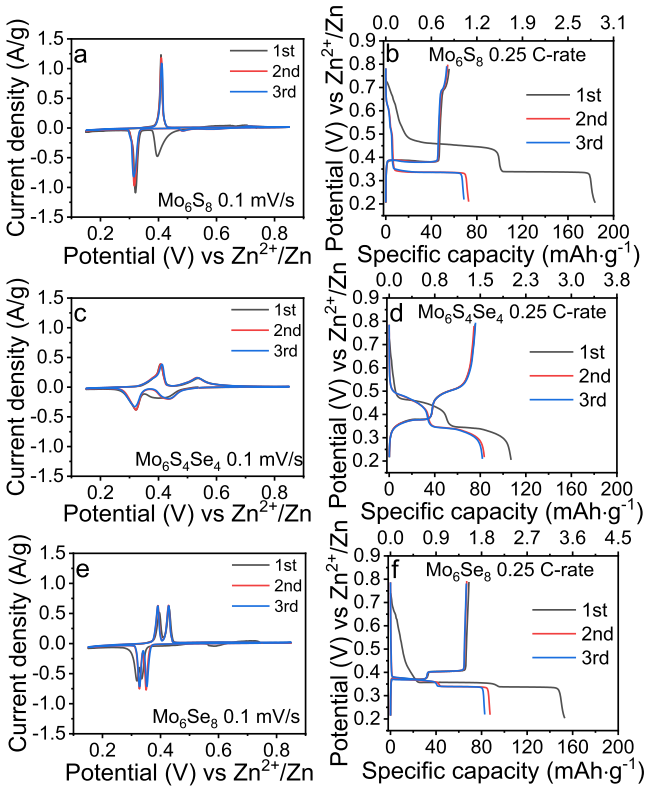

Figure 3. CV curves recorded at 0.1 mV/s and GCD profiles at 0.25 *C*-rate of (a,b) Mo_6S_8, (c,d) $Mo_6S_4Se_4$, and (e,f) Mo_6Se_8. All measurements started from OCV for the initial three cycles.

CV scans of these compounds, suggesting a difference in the insertion process compared to those of Mo_6S_8 (Figure 3a) and Mo_6Se_8 (Figure 3e) as discussed later. Furthermore, within the $Mo_6S_{8-x}Se_x$ (x = 2; 4; 6) series, the peaks associated with the insertion of Zn1 tend to appear at significantly higher voltages than that in the end members of the series. However, the theoretical voltages for the insertion of Zn1 and Zn2 into the relevant $Mo_6S_{8-x}Se_x$ compounds are consistent with the experimental values (Figure 2c), suggesting that the observed behavior is expected for the solid solution series. The experimental insertion voltages for Zn1 decrease as the Se-to-S ratio increases (showing a trend similar to the DFT results), while the voltage values for Zn2 remain broadly unchanged irrespective of the Se content. In this regard, $Mo_6S_2Se_6$ and Mo_6Se_8 show excellent reversibility in line with the DFT calculations of the binding energy (Figure 2a) which predicted that substituting S with Se would enable a fully reversible process down to fully deinserted chalcogenides.

The galvanostatic charge−discharge (GCD) curves of $Mo_6S_{8-x}Se_x$ (x = 0, 2, 4, 6, and 8) were recorded at 0.25 C (Figures 3 and S21, S22) and 1 C (Figure S23) rates to study the effect of the substitution on the specific capacity of the battery with the relevant data summarized in Table S5. Notably, taking the third cycle as a benchmark, the highest capacity (at rates of 1 and 2 C relevant to AZIB applications) is achieved by $Mo_6S_2Se_6$ rather than Mo_6Se_8. The same number of Zn is inserted into $Mo_6S_2Se_6$ as into Mo_6Se_8 (Figure 2d), suggesting that solid solution compounds are the way forward for reaching the optimal capacity.

Furthermore, consistent with the CV data, the GCD curves of Mo_6S_8 (Figure 3b) and Mo_6Se_8 (Figure 3f) exhibited flat plateaus at voltages similar to those in the CV scans and without obvious potential drops. However, for the three partially substituted Chevrel phases, the curves demonstrated a sloping form with the voltages continuing to increase/decrease along the whole charge/discharge stages, consistent with the broad peaks in the CV data. To test the possible origin of the slopes in GCD, we carried out in operando data studies on Mo_6S_8, $Mo_6S_4Se_4$, and Mo_6Se_8.

In Operando Studies of Zn-Ion Battery Performance of Mo_6S_8, $Mo_6S_4Se_4$, and Mo_6Se_8. The phase evolution of Zn insertion/deinsertion into Mo_6S_8 has been investigated by Chae et al.,[6] however, only using ex situ PXRD experiments. Therefore, to understand the variation of electrochemical performance with the increasing Se ratio, we carried out in operando PXRD studies combined with simultaneous GCD tests on Mo_6S_8, $Mo_6S_4Se_4$, and Mo_6Se_8 to examine the effect of electrochemistry on phase composition (Figure 4).

The measurements were carried out within a limited 2θ range to specifically target the most significant peaks pertinent to Mo_6S_8, $Mo_6S_4Se_4$, and Mo_6Se_8. In line with the electrochemical data, during the initial discharge plateau, the peaks

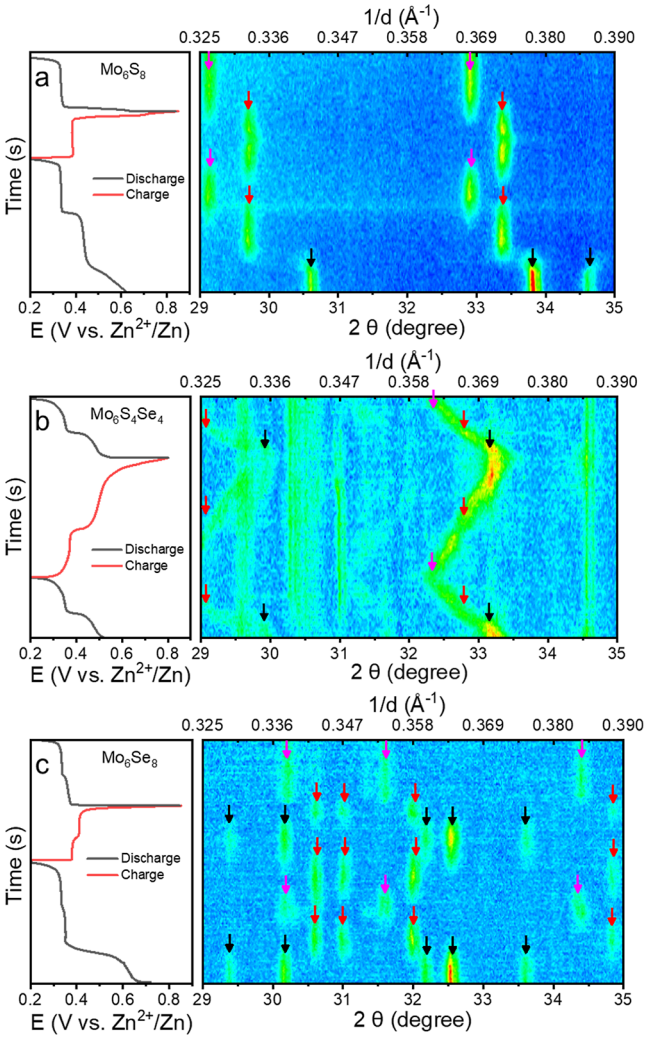

Figure 4. Contour plots of in operando XRD patterns and the accompanying charge/discharge curves (collected at 0.2 *C*-rate) of (a) Mo_6S_8, (b) $Mo_6S_4Se_4$, and (c) Mo_6Se_8. Black arrows mark the peaks of the pristine (uninserted) phases, and red and magenta arrows mark the peaks of the inserted phases with one zinc and two zinc ions, respectively.

https://doi.org/10.1021/acsami.4c09145
ACS Appl. Mater. Interfaces 2024, 16, 50671−50678

associated with Mo_6S_8 disappear, indicative of the Zn1 insertion and the appearance of the $ZnMo_6S_8$ peaks (Figure 4a). Subsequently, the second plateau is consistent with the formation of the $Zn_2Mo_6S_8$ phase, as evident from the X-ray diffraction. However, upon follow-up cycles, only peaks related to the $ZnMo_6S_8$ and $Zn_2Mo_6S_8$ (but not of Mo_6S_8) are visible, which is consistent with a partial deinsertion process.

Remarkably, the in operando data for $Mo_6S_4Se_4$ (Figure 4b) revealed different behavior. There is a gradual shift in the PXRD reflection positions upon cycling which suggests that a series of $Zn_{2-y}Mo_6S_4Se_4$ (y = 0−2) solid solutions are formed. The unit cell parameters and unit cell volume follow a gradual trend consistent with the formation of solid-state solutions upon Zn insertion (Figure S24). This is in stark contrast to Mo_6S_8 where discrete $ZnMo_6S_8$ and $Zn_2Mo_6S_8$ phases only exist. The formation of a solid solution explains the noticeable gradient in the charge−discharge curves for $Mo_6S_4Se_4$ compared to those observed for Mo_6S_8 and Mo_6Se_8 (Figure 3).

Contrary to Mo_6S_8, the in operando PXRD data show that the insertion of Zn into Mo_6Se_8 (Figure 4c) is fully reversible, as evidenced by the peaks of all three Mo_6Se_8, $ZnMo_6Se_8$, and $Zn_2Mo_6Se_8$ phase invariably being present in the diffraction patterns during the electrochemical process. However, these are discrete phases with no intermediate $Zn_{2-y}Mo_6Se_8$ phase being formed upon insertion. The comparison of unit cell parameters determined for the phase at the maximum insertion level further confirms its consistency with literature findings (Table S6), thus validating the reliability of the in operando experiment conducted in this work.

Thus, in operando experiments confirm the results of the ex situ electrochemical experiments and the results of the DFT calculations that due to significantly lower binding energies of Zn1 ions, it is possible to remove Zn ions fully from $ZnMo_6S_4Se_4$ and $ZnMo_6Se_8$. However, the striking difference in the insertion process, as evidenced by the distinctive slopes upon the insertion of $Mo_6S_4Se_4$ to $ZnMo_6S_4Se_4$ and the nearly horizontal plateaus in the case of the Mo_6Se_8 to $ZnMo_6Se_8$ process, requires additional explanation. Therefore, detailed DFT calculations were carried out to explain these phenomena.

Providing Explanation for a Gradual Insertion into $Mo_6S_4Se_4$. As noted above, unlike Mo_6S_8 and Mo_6Se_8, $Mo_6S_4Se_4$ does not show discrete phases formation upon insertion rather it forms continuous $Zn_yMo_6S_4Se_4$ (y = 0−1) solid solution phases (Figure 4b). To understand this unusual behavior of $Mo_6S_4Se_4$, DFT calculations were applied to determine the convex hull for Zn1 insertion into $Zn_yMo_6S_8$, $Zn_yMo_6S_4Se_4$, and $Zn_yMo_6Se_8$ across a range of y = 0−1 (Figure S25). In this framework, the aim was to determine the mixing energy per atom. Values of the mixing energy below the energy hull indicate that an intermediate phase is more stable. For example, in the case of y = 0.5, the corresponding mixing energy for $Zn_{0.5}Mo_6S_8$ is significantly above the energy hull, suggesting that $Zn_{0.5}Mo_6S_8$ is unstable and would be prone to phase separation into Mo_6S_8 and $Zn_1Mo_6S_8$. On the contrary, at y = 0.5, the resulting $Zn_{0.5}Mo_6S_4Se_4$ is below the energy hull, and thus, there is no tendency for it to segregate into $Zn_1Mo_6S_4Se_4$ and $Mo_6S_4Se_4$.

The results point out that there is a clear miscibility gap for Zn insertion in the case of Mo_6S_8, whereas intermediate Zn concentrations are only slightly unstable for Mo_6Se_8 indicating phase separation in agreement with the in operando XRD studies. In contrast, the $Mo_6S_4Se_4$ shows stable configurations at Zn contents of y = 0.5, resulting in a change of the mode of insertion to a solid solution in agreement with the charge−discharge profiles and in operando data.

CONCLUSIONS

In conclusion, the DFT calculations reveal that replacing more than two sulfur atoms with selenium in the $Mo_6S_{8-x}Se_x$ (x = 0−8) effectively lowers the binding energy of zinc ions, mitigating the ion trapping issues that have beset the battery performance of the parent Mo_6S_8 compound. Notably, the calculations suggest that further increasing the selenium content beyond the x = 2 threshold does not significantly enhance the binding energy reduction. Consequently, only a modest selenium substitution level is required to unlock the reversible zinc insertion and deinsertion behavior that is essential for high-performance aqueous zinc-ion battery cathodes. Experimental work confirms these findings with the cycling voltammetry on samples with x > 2 demonstrating distinctive peaks suggesting reversibility of Zn-ion insertion/deinsertion. The optimal performance was found for $Mo_6S_2Se_6$ that outperforms Mo_6Se_8 at battery relevant high charging rates. The combined in operando X-ray diffraction and electrochemical studies unveil a remarkable difference in the zinc insertion behavior between two end members (Mo_6S_8 and Mo_6Se_8) of the series and $Mo_6S_4Se_4$. Unlike the end members that undergo abrupt phase transitions into $ZnMo_6S_8$ and $ZnMo_6Se_8$ phases upon zinc insertion, $Mo_6S_4Se_4$ exhibits continuous solid solution behavior, forming $Zn_yMo_6S_4Se_4$ (y = 0−1) phases without abrupt phase transformation. This unusual characteristic of $Mo_6S_4Se_4$ was elucidated by DFT calculations that evaluated the mixing energy during zinc insertion. The computational results clearly highlight the existence of a miscibility gap for zinc insertion in Mo_6S_8, whereas $Mo_6S_4Se_4$ exhibits stable crystal structure configurations at zinc contents of y = 0.5, facilitating the formation of a continuous phase ranges. This fundamental difference in the insertion mechanism, arising from the tailored anion chemistry, is consistent with the charge−discharge profiles and in operando data. Overall, the synergistic combination of computational modeling and experimental validation provides valuable insights into optimizing the anion framework, paving the way for the development of advanced electrode materials with tailored properties for next-generation AZIBs.

ASSOCIATED CONTENT

Supporting Information

The Supporting Information is available free of charge at https://pubs.acs.org/doi/10.1021/acsami.4c09145.

Information regarding the materials, method of synthesis, and characterization; calculated molecular geometry; binding energy of solid solutions, Rietveld refinement of solid solutions; SEM images; EDXS spectra of solid solutions; battery test details; and mixing energies of solid solutions (PDF)

AUTHOR INFORMATION

Corresponding Authors

Axel Groß − *Institute of Theoretical Chemistry, Ulm University, 89081 Ulm, Germany; Helmholtz Institute Ulm (HIU) for Electrochemical Energy Storage, 89081 Ulm, Germany;* orcid.org/0000-0003-4037-7331; Email: axel.gross@uni-ulm.de

https://doi.org/10.1021/acsami.4c09145
ACS Appl. Mater. Interfaces 2024, 16, 50671−50678

Alexey Y. Ganin − *School of Chemistry, University of Glasgow, G12 8QQ Glasgow, U.K.;* orcid.org/0000-0002-3754-5819; Email: alexey.ganin@glasgow.ac.uk

Authors

Yuanshen Wang − *School of Chemistry, University of Glasgow, G12 8QQ Glasgow, U.K.*

Katharina Helmbrecht − *Institute of Theoretical Chemistry, Ulm University, 89081 Ulm, Germany*

Weihao Li − *School of Chemistry, University of Glasgow, G12 8QQ Glasgow, U.K.;* orcid.org/0000-0002-0388-7490

Manuel Dillenz − *Institute of Theoretical Chemistry, Ulm University, 89081 Ulm, Germany*

Yejun Wang − *School of Chemistry, University of Glasgow, G12 8QQ Glasgow, U.K.*

Complete contact information is available at: https://pubs.acs.org/10.1021/acsami.4c09145

Author Contributions

Yuanshen Wang, Katharina Helmbrecht, and Weihao Li contributed equally to this work. For the purpose of open access, the authors have applied a Creative Commons Attribution (CC BY) license to any Author Accepted Manuscript version arising from this submission. A.Y.G. and Y.W. designed the synthetic and electrochemical work. A.G., K.H., and W.L. designed, analyzed, and interpreted the results of DFT work with the help of M.D. Y.W. carried out the synthesis, characterization, and processing of the experimental data with the help of Y.W. (Yejun Wang) and W.L. The team was managed by A.Y.G. and A.G. All authors contributed to writing the manuscript and have granted their approval for the final version.

Funding

A.Y.G. acknowledges EPSRC (EP/W03333X/1) for supporting this work. W.L. acknowledges financial support by both China Scholarship Council and the University of Glasgow for Jim Gatheral Scholarship. Support by the German Research Foundation (DFG) under Germany's Excellence Strategy-EXC 2154-project no. 390874152 (POLiS Cluster of Excellence) is gratefully acknowledged. Computational resources have been provided by the state of Baden-Wuerttemberg through bwHPC and the German Research Foundation (DFG) through grant no. INST 40/575-1 FUGG (JUSTUS 2 cluster).

Notes

The authors declare no competing financial interest.

ABBREVIATIONS

AZIBs	aqueous zinc-ion batteries;
DFT	density functional theory
EDX	energy-dispersive X-ray
LIBs	lithium-ion batteries
CP	Chevrel phase
CV	cyclic voltammetry
GCD	galvanostatic charge−discharge
PBE	Perdew−Burke−Ernzerhof
RPBE + D3	revised PBE functional in combination with the Grimme D3 correction
PXRD	powder X-ray diffraction
SEM	scanning electron microscope
XRD	X-ray diffraction

REFERENCES

(1) McLarnon, F. R.; Cairns, E. J. The secondary alkaline zinc electrode. *J. Electrochem. Soc.* **1991**, *138*, 645−656.
(2) Tarascon, J. M.; Armand, M. Issues and challenges facing rechargeable lithium batteries. *Nature* **2001**, *414*, 359−367.
(3) Kang, K.; Meng, Y. S.; Bréger, J.; Grey, C. P.; Ceder, G. Electrodes with high power and high capacity for rechargeable lithium batteries. *Science* **2006**, *311*, 977−980.
(4) Chevrel, R.; Hirrien, M.; Sergent, M. Superconducting Chevrel phases: prospects and perspectives. *Polyhedron* **1986**, *5*, 87−94.
(5) Mei, L.; Xu, J.; Wei, Z.; Liu, H.; Li, Y.; Ma, J.; Dou, S. Chevrel phase Mo_6T_8 (T= S, Se) as electrodes for advanced energy storage. *Small* **2017**, *13*, 1701441.
(6) Chae, M. S.; Heo, J. W.; Lim, S. C.; Hong, S. T. Electrochemical zinc-ion intercalation properties and crystal structures of $ZnMo_6S_8$ and $Zn_2Mo_6S_8$ chevrel phases in aqueous electrolytes. *Inorg. Chem.* **2016**, *55*, 3294−3301.
(7) Cheng, Y.; Luo, L.; Zhong, L.; Chen, J.; Li, B.; Wang, W.; Mao, S. X.; Wang, C.; Sprenkle, V. L.; Li, G.; Liu, J. Highly reversible zinc-ion intercalation into chevrel phase Mo_6S_8 nanocubes and applications for advanced zinc-ion batteries. *ACS Appl. Mater. Interfaces* **2016**, *8*, 13673−13677.
(8) Levi, M. D.; Lancri, E.; Levi, E.; Gizbar, H.; Gofer, Y.; Aurbach, D. The effect of the anionic framework of Mo_6X_8 Chevrel Phase (X= S, Se) on the thermodynamics and the kinetics of the electrochemical insertion of Mg^{2+} ions. *Solid State Ionics* **2005**, *176*, 1695−1699.
(9) Helmbrecht, K.; Euchner, H.; Groß, A. Revisiting the chevrel phase: Impact of dispersion corrections on the properties of Mo_6S_8 for cathode applications. *Batteries Supercaps* **2022**, *5*, e202200002.
(10) Jadhav, A. L.; Juran, T. R.; Kim, M. A.; Bruck, A. M.; Hawkins, B. E.; Gallaway, J. W.; Smeu, M.; Messinger, R. J. Reversible electrochemical anionic redox in rechargeable multivalent-ion batteries. *J. Am. Chem. Soc.* **2023**, *145*, 15816−15826.
(11) Hohenberg, P.; Kohn, W. Inhomogeneous electron gas. *Phys. Rev.* **1964**, *136*, B864−B871.
(12) Kohn, W.; Sham, L. J. Self-consistent equations including exchange and correlation effects. *Phys. Rev.* **1965**, *140*, A1133−A1138.
(13) Kresse, G.; Hafner, J. Ab initio molecular dynamics for liquid metals. *Phys. Rev. B: Condens. Matter Mater. Phys.* **1993**, *47*, 558−561.
(14) Kresse, G.; Furthmüller, J. Efficient iterative schemes for ab initio total-energy calculations using a plane-wave basis set. *Phys. Rev. B: Condens. Matter Mater. Phys.* **1996**, *54*, 11169−11186.
(15) Kresse, G.; Joubert, D. From ultrasoft pseudopotentials to the projector augmented-wave method. *Phys. Rev. B: Condens. Matter Mater. Phys.* **1999**, *59*, 1758−1775.
(16) Perdew, J. P.; Burke, K.; Ernzerhof, M. Generalized gradient approximation made simple. *Phys. Rev. Lett.* **1996**, *77*, 3865−3868.
(17) Cho, J. H.; Ha, J. H.; Lee, J. G.; Kim, C. S.; Cho, B. W.; Kim, K. B.; Chung, K. Y. Systematic investigation into Mg^{2+}/Li^{+} dual-cation transport in Chevrel phases using computational and experimental approaches. *J. Phys. Chem. C* **2017**, *121*, 12617−12623.
(18) Zhang, Y.; Yang, W. Comment on "Generalized gradient approximation made simple. *Phys. Rev. Lett.* **1998**, *80*, 890.
(19) Grimme, S.; Ehrlich, S.; Goerigk, L. Effect of the damping function in dispersion corrected density functional theory. *J. Comput. Chem.* **2011**, *32*, 1456−1465.
(20) Euchner, H.; Groß, A. Atomistic modeling of Li-and post-Li-ion batteries. *Phys. Rev. Mater.* **2022**, *6*, 040302.
(21) Selwyn, L. S.; McKinnon, W. R.; Dahn, J. R.; Le Page, Y. Local environment of Li intercalated in $MoSe_zS_{8-z}$ as probed using electrochemical methods. *Phys. Rev. B: Condens. Matter Mater. Phys.* **1986**, *33*, 6405−6414.
(22) Belin, S.; Burel, L.; Chevrel, R.; Sergent, M. Self-molybdenum intercalation: stabilization of metastable pseudo-binary Chevrel phases in Mo_6Se_8−Mo_6S_8 system. *Mater. Res. Bull.* **2000**, *35*, 151−168.
(23) McGuire, M. A.; Ranjan, C.; DiSalvo, F. J. $Cu_4Mo_6Se_8$: synthesis, crystal structure, and electronic structure of a new chevrel phase structure type. *Inorg. Chem.* **2006**, *45*, 2718−2726.

(24) Tarascon, J. M.; Di Salvo, F. J.; Waszczak, J. V.; Hull, G. W. Synthesis and peculiar properties of $InMo_6S_{8-x}Se_x$, $TlMo_6S_{8-x}Se_x$, and $Hg_yMo_6S_{8-x}Se_x$. *Phys. Rev. B: Condens. Matter Mater. Phys.* **1985**, *31*, 1012−1021.
(25) Tarascon, J. M.; DiSalvo, F. J.; Murphy, D. W.; Hull, G.; Waszczak, J. V. New superconducting ternary molybdenum chalcogenides $InMo_6Se_8$, $T1Mo_6S_8$, and $TlMo_6Se_8$. *Phys. Rev. B: Condens. Matter Mater. Phys.* **1984**, *29*, 172−180.
(26) Okubo, M.; Hosono, E.; Kim, J.; Enomoto, M.; Kojima, N.; Kudo, T.; Zhou, H.; Honma, I. Nanosize effect on high-rate Li-ion intercalation in $LiCoO_2$ electrode. *J. Am. Chem. Soc.* **2007**, *129*, 7444−7452.

https://doi.org/10.1021/acsami.4c09145
ACS Appl. Mater. Interfaces 2024, 16, 50671−50678